Front. Med. 2025, 19(3): 493−506
https://doi.org/10.1007/s11684-025-1128-4

RESEARCH ARTICLE

Identification of a nanobody able to catalyze the destruction of the spike-trimer of SARS-CoV-2

Kai Wang[1,*], Duanfang Cao[2,*], Lanlan Liu[1,3,*], Xiaoyi Fan[2,3,*], Yihuan Lin[1], Wenting He[2,3], Yunze Zhai[4], Pingyong Xu[2,3], Xiyun Yan[2,3], Haikun Wang (✉)[4], Xinzheng Zhang (✉)[2,3], Pengyuan Yang (✉)[1,3,#]

[1]Key Laboratory of Epigenetic Regulation and Intervention, Institute of Biophysics, Chinese Academy of Sciences, Beijing 100101, China; [2]National Laboratory of Biomacromolecules, CAS Center for Excellence in Biomacromolecules, Institute of Biophysics, Chinese Academy of Sciences, Beijing 100101, China; [3]University of Chinese Academy of Sciences, Beijing 100049, China; [4]State Key Laboratory of Cardiology and Medical Innovation Center, Shanghai East Hospital, School of Medicine, Tongji University, Shanghai 200120, China

Abstract **Neutralizing antibodies have been designed to specifically target and bind to the receptor binding domain (RBD) of spike (S) protein to block severe acute respiratory syndrome coronavirus 2 (SARS-CoV-2) virus from attaching to angiotensin converting enzyme 2 (ACE2). This study reports a distinctive nanobody, designated as VHH21, that directly catalyzes the S-trimer into an irreversible transition state through postfusion conformational changes. Derived from camels immunized with multiple antigens, a set of nanobodies with high affinity for the S1 protein displays abilities to neutralize pseudovirion infections with a broad resistance to variants of concern of SARS-CoV-2, including SARS-CoV and BatRaTG13. Importantly, a super-resolution screening and analysis platform based on visual fluorescence probes was designed and applied to monitor single proteins and protein subunits. A spontaneously occurring dimeric form of VHH21 was obtained to rapidly destroy the S-trimer. Structural analysis via cryogenic electron microscopy revealed that VHH21 targets specific conserved epitopes on the S protein, distinct from the ACE2 binding site on the RBD, which destabilizes the fusion process. This research highlights the potential of VHH21 as an abzyme-like nanobody (nanoabzyme) possessing broad-spectrum binding capabilities and highly effective anti-viral properties and offers a promising strategy for combating coronavirus outbreaks.**

Keywords nanobody; SARS-CoV-2; spike-trimer; catalyzation; rapid destruction

Introduction

Since the onset of coronavirus disease (COVID-19) pandemic, the severe acute respiratory syndrome coronavirus 2 (SARS-CoV-2) genome has undergone rapid and continuous evolution through the accumulation of mutations [1]. The Omicron variant exhibits over 30 amino acid substitutions in its spike (S) protein, which surpasses the number found in the original SARS-CoV-2 strain, with 15 of these changes occurring in the receptor binding domain (RBD) [2,3]. Notably, the BA.4 and BA.5 subvariants of SARS-CoV-2 Omicron are rapidly expanding due to additional S mutations that alter antibody evasion properties. Sera from vaccinated and previously infected individuals exhibit a reduced neutralizing capacity against these Omicron subvariants, and monoclonal antibodies (mAbs) that were effective against the original variant are now largely ineffective against these new subvariants [4]. This scenario underscores the threat posed by SARS-CoV-2 Omicron subvariants to public health and the urgent need for interventions, such as broad-spectrum antibodies, that can address the evolving landscape of SARS-CoV-2 variants resulting from antigenic shifts.

Similar to that of other coronaviruses, the entry of SARS-CoV-2 into host cells is mediated by the transmembrane S protein, which forms homotrimers protruding from the viral surface. The S protein facilitates viral membrane fusion, which allows virus entry into host cells, and can form several conformational transition

Received June 5, 2024; accepted December 16, 2024

Correspondence: Haikun Wang, hkwang@tongji.edu.cn;
Xinzheng Zhang, xzzhang@ibp.ac.cn;
Pengyuan Yang, pyyang@ibp.ac.cn

*These authors contributed equally to this work.
#Lead contact.

states [5]. A furin cleavage site located at the junction of the S1/S2 subunits is spontaneously processed by proteases during viral assembly within host cells [6]. During the infection process, the S-trimer undergoes irreversible conformational changes, which leads to the release of the S1 subunit following angiotensin converting enzyme 2 (ACE2) receptor binding to the RBD domain. This process enables the S2 subunit to insert the internal fusion peptide into target cells and facilitates fusion between the virus membrane and host cells [7]. Although most known conventional neutralizing antibodies and nanobodies target the S protein RBD domain of the S protein [8–14], the Omicron variant has demonstrated a notable resistance to existing SARS-CoV-2 neutralizing mAbs, which often target diverse epitopes [3,15–17]. Post-acute and long-term sequelae of the COVID-19 pandemic requires the development of potent antibodies that can target novel conserved epitopes with a broad-spectrum activity against evolving viral strains [17–19].

Recent emerging evidence suggests that neutralizing antibodies of SARS-Cov-2 may directly disrupt S-trimer integrity and represents a new mechanism for blocking viral infection [20]. A broad-neutralizing monomeric nanobody obtained via the rapid triggering of S-trimer depolymerization has not been reported. However, the mechanisms underlying antibody disruption remain complex and challenging to predict. An intuitive and effective method for the observation of the dynamic process and efficiency of S-trimer depolymerization within minutes is lacking. Building on previous studies suggesting that catalytic activity can reside in the variable domain of antibodies [21], a growing interest focuses on the exploration of the potential of nanobodies to exhibit a catalytic activity due to their small size and spatial proximity to antigens. In this study, we developed a visual fluorescence probe platform based on double fluorescent labeling of nanobodies and target proteins. Following the same principles and mechanisms, imaging assay was used to screen and identify nanobodies that can disrupt the S-trimer by employing different high-resolution microscopes. Among the candidate neutralizing nanobodies identified, a spontaneous dimeric nanobody named VHH21 catalyzes conformational changes in the S-trimer of SARS-CoV-2, which leads to rapid disruption of the prefusion state. Structural analyses using cryo-electron microscopy (Cryo-EM) and structural prediction techniques revealed that VHH21 drives the S-trimer toward a postfusion conformation, which accelerated its destruction. Furthermore, VHH21 binds to a novel and highly conserved epitope, which confers resistance against diverse SARS-CoV-2 variants, and related viruses, such as SARS-CoV and BatRaTG13. The visual fluorescence probe platform can be applied to the screening and identification of catalytically active compounds or proteins and the study of depolymerization mechanisms in the future.

Materials and methods

Camel immunization

Two 2-year-old Bactrian camels were purchased from the Longhui Corporation (Shandong, China). The camels were immunized with 200 μg of each immunogen. Peripheral blood was collected for enzyme-linked immunosorbent assay (ELISA) studies, lymphocyte cell extraction, and phage library construction. The experimental procedures for use and care of animals were approved by the ethics committee of Institute of Biophysics, Chinese Academy of Sciences.

ELISA

The ELISA plate was coated with different S1 proteins and blocked with gelatin. A serial dilution of serum or VHH was added for 1 h, followed by the addition of goat anti-llama horse radish peroxidase (HRP) or rat anti-Hemagglutinin (HA) tag-HRP antibodies. The plate was washed using phosphate buffered saline-buffer supplemented with 0.02% (v/v) Tween-20 (PBST) after each of the step above. Finally, 3,3′,5,5′-tetramethylbenzidine (TMB) solution was added, and the reaction was terminated using H_2SO_4. The absorbance was read at 450 nm on a microtiter plate reader (ELX80, BioTek). ELISA data were analyzed through nonlinear regression using GraphPad Prism 8.

The competitive and phage ELISA methods were performed similarly as mentioned above. A mixture of rabbit anti-FD bacteriophage antibody and goat anti-rabbit HRP antibody was used for phage ELISA. For competitive ELISA, threefold serial dilutions of S1 protein were added to the plate, and the serum was added subsequently.

Phage displaying VHH library construction

Total mRNA was extracted in accordance with the protocol of LeukoLOCK^{TM} Total RNA Isolation System. The VHH regions were amplified from the transcribed cDNA based on a series of classic primers [22,23] and a novel reverse primer (VHH-R3). These regions and plasmid pComb3X (generously provided by Dr. Barbas) were digested and ligated together using the restriction enzyme *Sfi* I and T4 DNA Ligase. The ligated product was then electroporated into competent cells of *E. coli* ER2738. M13KO7 helper phages were added to the cells, and VHH-displaying phages were precipitated and resuspended after amplification overnight. The characteristics of VHH libraries were ensured through

measurement of colony-forming units, colony–polymerase chain reaction sequencing, and plaque-forming units.

Biopanning for S-directed nanobodies

Our method for nanobody isolation is based on our previous study [24]. A streptavidin-preprocessed 96-well plate was coated with biotinylated RBD or S1 and blocked with bovine serum albumin (BSA). The mixed two phage-displaying VHH libraries were added to the panning wells. After washing, the panning wells were eluted with RBD or S1(D614G) as the competing target. The eluent was transferred in equal aliquots to the next four BSA-coated wells to remove non-specifically phages. Then the eluent was collected from the wells and amplified with addition of the M13KO7 helper phage for the next round of panning. The entire panning process was repeated for three rounds.

Expression and purification of S-directed nanobodies

VHHs were expressed in *E. coli* TOP10F, in accordance with previously reported methods [24]. The protein eluted from Ni-NTA was concentrated and further purified via gel filtration chromatography using a Superdex 200 increase 10/300 column QHP column (GE Healthcare) to remove contaminants.

Biolayer interferometry (BLI) assay

In the BLI assay, the biotinylated RBD and S1 proteins were immobilized onto streptavidin-coated biosensors (Octet, ForteBio) pre-equilibrated in assay buffer (PBST). The assay involved baseline, association, and dissociation steps. The data were then analyzed using a 1:1 binding model for equilibrium dissociation constant (K_D), association constant (Ka), and dissociation constants (Kd) calculations using the built-in software Data Analysis 10.0.

For competition binding capacity assay, immobilization was performed as described above. The sensors were sequentially incubated with the VHHs or ACE2 simultaneously.

Pseudovirus neutralization assay

The cDNAs of the S proteins mentioned above were synthesized and inserted into pcDNA3.1$^+$ vector by Beijing DIA-UP Biotechnology Co., Ltd. Pseudovirus neutralization assay was performed as previously described [25]. The infection percentage was calculated using the formula: Infection (%) = ((sample RLU− blank RLU)/(positive control RLU−blank RLU)) (%). The positive control RLU was derived from cells infected with SARS-CoV-2 pseudotyped virus in the absence of nanobodies. The half-maximal effective concentration of nanobodies (EC_{50}) was determined through four-parameter nonlinear regression (GraphPad Prism 8).

Expression and purification of SARS-CoV-2 S-trimer

The SARS-Cov-2 S gene (GenBank accession number: MN908947; residues: 14–1208) was synthesized. Transfer vector design and construction, virus transfection and amplification, and expression and purification of the recombinant S protein were performed as previously reported [26]. The expression and purification methods of mutant were the same as above.

Functional screening of destructive nanobodies

During screening, the mouse anti-S2 antibody was coated onto 96-well glass plates and blocked with 3% (BSA). The S-trimer was added, followed by the rabbit anti-S1 (NTD) primary antibody and Alexa Fluor 555-labeled donkey antirabbit secondary antibody. VHHs or ACE2 was incubated with the mouse anti-HIS tag primary antibody and Alexa Fluor488-labeled goat anti-mouse secondary antibody. Confocal images were obtained using an Olympus IXplore SpinSR microscope, and Image J software was used to analyze the number of red fluorescently labeled S1 before and after the addition of VHH/ACE2. The destruction rate heat map was plotted via GraphPad Prism 8.

Fluorescence super-resolution imaging assay

Coating, blocking, and VHH/ACE2 fluorescent labeling were performed as described above. Abberiors STAR RED goat antirabbit antibody and Abberiors STAR ORANGE goat antimouse antibody were substituted for Alexa Fluor 555-labeled donkey antirabbit antibody and Alexa Fluor 488-labeled goat antimouse antibody, respectively. Confocal and stimulated emission depletion (STED) images were obtained using a STEDYCON equipped with an inverted Nikon microscope. Total internal reflection fluorescent microscopy (TIRFM) images were acquired using a homemade TIRF microscopy system and Andor Solis software [27].

Gel-filtration chromatography analysis

The purified S-trimer was cleaved with thrombin and furin to remove the C-terminal trimerization domain and His_6-tag and cleave the S1/S2 cleavage site. The first round of gel filtration chromatography was conducted to purify the cleaved product using a pre-equilibrated Superdex 200 10/300 column. Most of the cleaved S1 and S2 subunits remained as trimers in prefusion state, and they were collected and mixed with VHH21 at a mole

ratio of 1:4. After incubation at 4 °C for 10 min, the mixtures were centrifuged and loaded onto the Superdex 200 10/300 column again. The eluted proteins from gel-filtration chromatography were analyzed via sodium dodecyl sulfate polyacrylamide gel electrophoresis (SDS-PAGE) and negative staining.

Negative-staining electron microscopy

VHH/S-trimer complexes were adsorbed onto a glow-discharged carbon layer (EMCN). After incubation, washing, and staining, the samples were screened using an FEI Tecnai Spirit electron microscope operating at an acceleration voltage of 120 kV.

Cryo-EM sample preparation and data collection

The cryo-EM sample (VHH21/S-trimer complex) was prepared immediately after the addition of VHH21 to the fixed WT S protein at a molar ratio of 3:1. The complex with a final concentration of the WT S at 0.7 mg/mL was placed on a glow-discharged grid (GIG, 400 mesh, R1/1). The grid was blotted and plunge-frozen in liquid ethane using an automatic plunge freezer (Leica EM GP). All cryo-EM single-particle data were collected on Titan Krios transmission electron microscopes (Thermo Scientific) operating at 300 kV through the beam-image shift data collection method [28].

Cryo-EM data processing

Movie stacks were processed for beam-induced motion correction using MotionCor2 [29]. Images without dose weighting were used to determine the contrast transfer function through the program CTFFIND4 [30]. Further data processing was conducted on dose-weighted images using RELION 3 [31]. A bulk of particles was autopicked and subjected to several rounds of two-dimensional (2D) classification. Well-defined particles were retained for 3D classifications, with the map generated by PDB 7DK3 used as the initial model. The particles of the S-trimer bound to two VHH21 were selected for another round of 3D classification, and four out of five classes with good features were retained for subsequent 3D autorefinement with C1 symmetry. Finally, only the particles whose densities were around that of the VHH21 and its bound RBD in the down conformation and the adjacent NTD were retained. The resolution was estimated based on the gold-standard Fourier shell correlation, and the local resolution of the maps were measured using ResMap [32].

Cryo-EM model construction

For model construction, a previously reported structure of SARS-CoV-2 S-trimer in prefusion state (PDB: 7DK3) and the structures of VHH21 predicted by AlphaFold [33] were docked to the cryo-EM maps using UCSF Chimera [34]. Models including all the regions of the S-trimer, except for the up-RBD and the region of VHH21 bound to the down-RBD, were iteratively rebuilt in Coot [35] and subjected to real-space refinement in Phenix [36]. The refined model of the down-RBD bound to the VHH21 was selected and fitted into the densities of the half-up RBD and its interacting VHH21 in the map, and the overall model was further refined using Phenix. The geometries of the structure were evaluated using MolProbity [37]; Table S1 summarizes the parameters of cryo-EM data collection and refinement statistics.

Mass spectrum

The purified VHH21 sample was analyzed using a quadrupole time-of-flight (TPF) mass spectrometer consisting of a high-performance liquid chromatograph (HPLC) connected to a TOF mass spectrometer. In brief, 3 μL sample was loaded into the HPLC column (300SB-C8, 2.1 mm× 50 mm; 3.5 μm particle) and separated using a 2%–98% linear gradient in 10 min at a flow rate of 0.2 mL/min. The eluted samples were introduced online into the mass spectrometer through nanoelectrospray ionization, and the data within 600–2400 *M/Z* were selected for mass analysis (Fig. S1).

Results

Isolation and identification of S-directed nanobodies

To develop highly potent broad-spectrum nanobodies, we employed immunization strategies and VHH library construction designs. The Bactrian camels were subcutaneously immunized with an emulsified immunogen mixture comprising various recombinant S proteins, including full-length, S1, and the RBD domain (Fig. 1A). This mixture stimulated the serum with a strong cross-reactivity and affinity for S and S1 proteins of diverse coronaviruses tested, including all five types of SARS-CoV-2 variants of concern (VOCs), and BatRaTG13, SARS-CoV, Middle East respiratory syndrome CoV (MERS-CoV), and Human-CoV (Figs. 1B, 1C, S2B, and S2C). We constructed two high-quality and diverse phage-displaying VHH libraries with satisfactory parameters (Fig. S2D and S2E; Table S2) and identified six positive nanobodies with a binding activity for the S1 proteins of coronaviruses mentioned above (Figs. 1D and S2F–S2H), with a substantial sequence diversity in the complementarity-determining region (CDR) sequences (Fig. S2I and S2J). Notably, VHH21 was characterized by spontaneous dimerization during protein purification (Fig. S1).

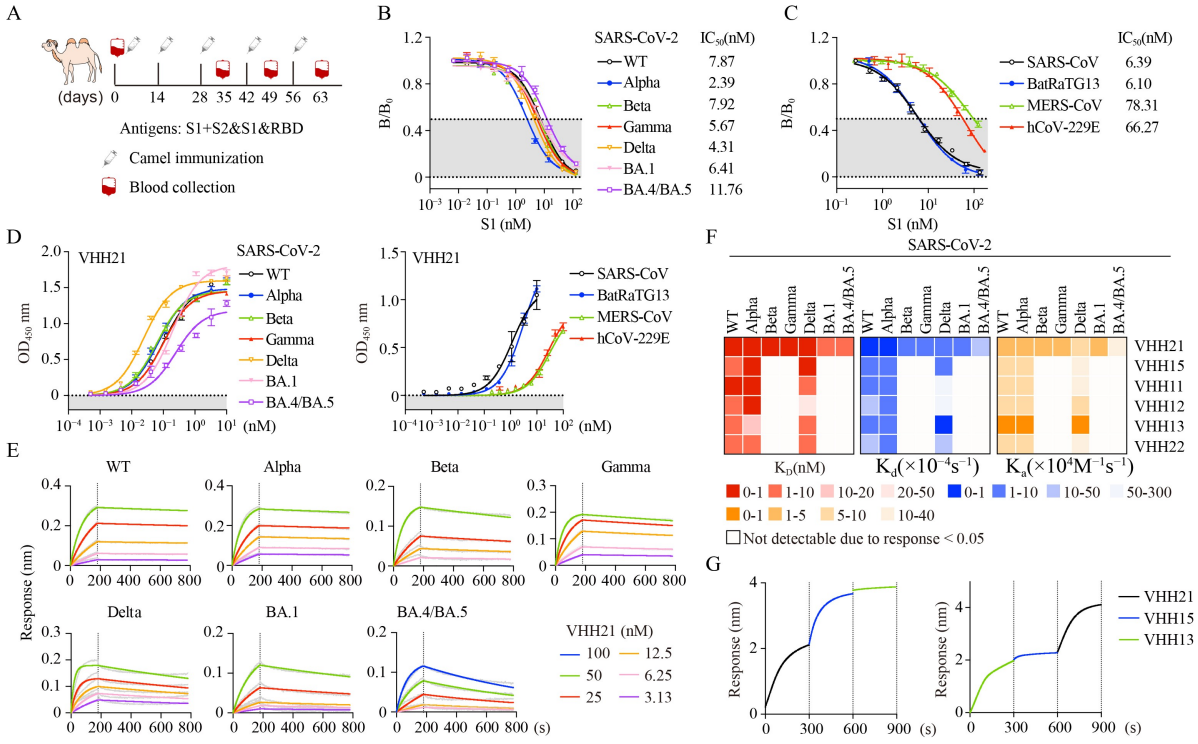

Fig. 1 Immunization and isolation of nanobodies against SARS-CoV-2. (A) Immunization of two Bactrian camels and peripheral blood collection to obtain high-affinity nanobodies against SARS-CoV-2. (B–C) Affinity of the camel 5th-immunization serum to the S1 proteins of SARS-CoV-2 variants, SARS-CoV, BatRaTG13, MERS-CoV, and hCoV-229E was quantified through competitive ELISA. Normalized values from three independent experiments are expressed as mean ± standard deviation (SD), and half maximal inhibitory concentration values are plotted. (D) Binding capacity assays of VHH21 performed through VHH ELISA, which showed cross-reactivity to the S1 proteins mentioned above. Data points represent the mean ± SD of three independent experiments. (E) BLI analysis of the affinity of VHH21 for the S1 proteins mentioned above; 15 μg/mL biotinylated S1 was immobilized on an Octet SA sensor. VHH at different concentrations was associated for 180 s, followed by dissociation for 600 s. The gray trace represents raw data, and the colored lines show fitted curves applying a 1:1 interaction model. The K_D displayed in Table S3 were determined from the fitting. Representative binding curves were obtained from three independent experiments. (F) Heat maps revealing the affinity profile of six VHH candidates for virous S1 proteins. (G) BLI response analysis of the competitive binding of VHHs to SARS-CoV-2 WT RBD proteins; 2 g/mL biotinylated SARS-CoV-2 WT RBD protein was immobilized on an Octet SA sensor. Then, binding to each VHH was investigated with association for 300 s but without the dissociation process. Representative binding curves are shown from three independent experiments.

To quantify the binding affinity of the selected nanobodies to S1 proteins, we used BLI to measure the binding-curve kinetics (Figs. 1E and S3). Consistent with the ELISA binding curves, VHH21 exhibited single or less nanomolar levels of affinity for all the S1 proteins of SARS-CoV-2 VOCs, with K_D values ranging from 0.32 to 7.89 nmol/L. Importantly, VHH21 affinities toward all VOC S1 proteins showed no sign of evident reduction (Fig. 1F; Table S3), and almost no dissociation was observed over 10 min, which indicates the high sensitivity and potential high stability of the VHHs (Fig. 1E; Table S3). Given the high sequence similarity and identical results of VHH15, VHH11, VHH12, and VHH22 (Fig. S2J), we selected VHH15 with the best affinity as a representative for comparative presentation with VHH13 and VHH21. In a BLI-based competition binding assay for the immobilized RBD and S1 of SARS-CoV-2, VHH21 showed no competition with other VHH candidates, which implies its recognition of diverse potential epitopes (Figs. 1G and S4).

Functional screening and identification of S-trimer destructive nanobody

To obtain destructive nanobodies, we employed a visual fluorescence super-resolution imaging assay using confocal microscope to screen the destructive nanobodies from the above candidate neutralizing nanobodies. S-Trimers were coated on the bottom of microscopy-grade plate and labeled by Alexa fluor 555™ (red) conjugated anti-NTD domain antibody. Then, the VHHs or ACE2 protein labeled by Alexa fluor 488™ (green) conjugated anti-his antibody were added to the medium and washed immediately at 1 and 20 min (Fig. 2A). Fluorescence data were captured via confocal microscopy, and the super-resolution images were analyzed. The disruption rate of the S-trimer was calculated using Image J software. VHH21 ranked the top in terms of the capability to

destruct S-trimer among these neutralizing antibodies, with 68% of the S-trimer destroyed within 20 min (Fig. 2B). To confirm the destructive capability of VHH21, we used negative staining to analyze changes in the S-trimers when complexed with nanobodies. Negative-staining analysis revealed no visible changes in the vast majority of the complexes with six nanobodies and ACE2. Only the complexes with VHH21 showed a significant decrease in the number and led to complete dissociation of the S-trimer (Fig. 2C). These data demonstrate that VHH21 can rapidly destruct the S-trimer.

Verification of rapid destruction of the S-trimer by VHH21

To further verify the destructive capability of VHH21, we used size-exclusion chromatography (SEC) and negative staining to analyze changes in the S-trimer when complexed with nanobodies. Consistent with previous reports [38], most precleaved S proteins were eluted in peak S with S1 and S2 assembly, which indicates the noncovalently associated S-trimers in the prefusion state (Fig. 3A–3C). Subsequently, the peak S was collected, complexed with each nanobody, and subjected to a second round of SEC. Figure 3A shows that a small percentage of the S-trimers retained the prefusion conformation, and the majority of the proteins were eluted from additional peaks after the treatment with VHH21. These outcomes imply a conformational transition in the S-trimers. Following the separation of each peak component using SDS-PAGE and negative staining, we identified peaks 2 and 3, which eluted after peak S, as the S1 subunit bound to VHH21 and the S2 subunit alone, respectively. These components eluted in peaks 2 and 3 likely represent monomeric proteins due to their late peak position. Negative-staining analysis revealed that the vast majority of the complexes with the VHH21 appeared as clusters of small particles (Fig. 3C). Altogether, these results indicate that VHH21 catalyzed conformational changes in the S-trimer and disrupted the prefusion state.

To further evaluate how VHH21 catalyzed the pulling down of the S1 domain in the S-trimer, we employed a STED microscope, following the same method as confocal microscopy, to monitor the conformational changes. Upon the addition of nanobodies (green), the S-trimers (light purple) were rapidly disrupted, and a large amount of snowflake S1/VHH complexes (bright white) drifting away was observed immediately. This phenomenon did not occur in the wells with ACE2 (Figs. 3D and S5, Movie S1). To monitor the destruction efficiency, we used a visual TIRF microscope assay, with imaging time intervals set up to 50 ms. This condition provided 20 microscopy images per second. The S1/VHH complexes immediately drifted away and moved within this 50 ms interval (Movie S2). These data further demonstrate that these nanobodies catalyzed the rapid destruction of the S-trimer prefusion state.

Broad neutralizing capacity against S pseudoviruses

To evaluate the neutralizing capacities of the isolated nanobodies, we used pseudotyped lentivirus (PSV) harboring a luciferase reporter with SARS-CoV-2 VOCs S to infect ACE2 - overexpressing 293T cells (Fig. 4A and 4B) [39]. The candidate nanobodies displayed strong

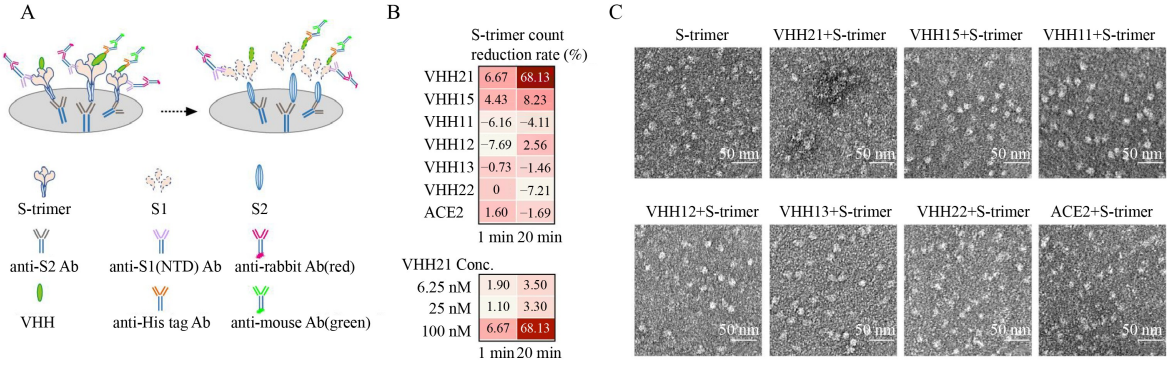

Fig. 2 Functional screening and identification of S-trimer destructive nanobodies. (A) Visual fluorescence super-resolution imaging assay was used to select the destructive nanobodies from the positive candidates. Antirabbit antibody (red), and anti-mouse antibody (green) were mixed with rabbit anti-S1 (NTD) antibody and mouse anti-his tag antibody, respectively, used to stain the S1-NTD domain of the S-trimer and VHHs. (B) Confocal images were recorded before and after addition of the stained 100 nmol/L VHHs or ACE2 complexes at 1 and 20 min. A total of 6.25, 25, and 100 nmol/L VHH21 were used to compare the effect of concentration. The number of S-trimer and destruction rate calculations were obtained using Image J software 13.0. The disruption rate was calculated using the formula: disruption rate (%) = ((S1 counts before added−S1 counts after added)/S1 counts before added) (%). (C) Negative-staining analysis of VHH/S-trimer complexes. Exactly 0.03 mg/mL S-trimers were mixed with VHHs at a 1:4 molar ratio for 10 min at 4 °C. A total of 5 μL complexes were added to the grid and incubated for 1 min, and excess sample was wiped off using filter paper. Then, the grid was stained with 5 μL 2% uranyl acetate solution for 1 min. Scale bar: 50 nm.

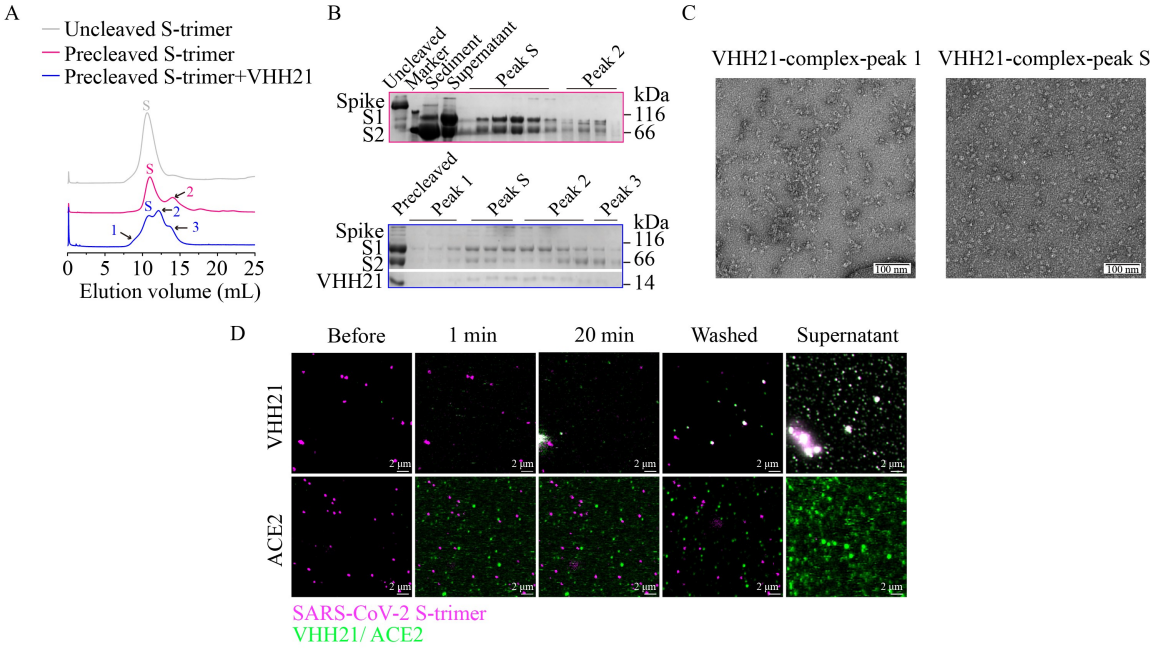

Fig. 3 Nanobodies catalyzed the release of S1 and conformational changes in the S-trimer. (A) Gel filtration profiles of S-trimer (gray), S-trimer digestion by thrombin and furin (magenta), and destroyed S-trimer bound to VHH21 (blue). The purified S proteins were cleaved with thrombin and furin overnight at 16 °C. Then, the precleaved S-trimers were mixed with VHH21 at a 1:4 molar ratio for 10 min at 4 °C. (B) SDS-PAGE results of S-trimer digestion by thrombin and furin (magenta box) and destroyed S-trimer bound to VHH21 (blue box). (C) Negative-staining analysis of peaks 1 and S in the gel filtration profiles of precleaved S-trimers bound to VHH21; 5 μL protein at a concentration of 0.03 mg/mL was added onto the grid and incubated for 1 min. Excess sample was wiped off using a filter paper. Then, the grid was stained with 5 μL 2% uranyl acetate solution for 1 min. Scale bar: 100 nm. (D) Immunofluorescence assay confirming that VHH21 can rapidly destroy the S-trimer. Immobilized, staining S-trimer complexes (light purple) were treated with staining VHH21 or ACE2 complexes (green) as a control group. Confocal images (pixel size: 100 nm) were recorded before and after the addition of the stained VHH or ACE2 complexes every 1 min for 20 min. The bottom of the plate was washed, and the supernatant obtained after addition of the stained VHH or ACE2 complexes was transferred to a new empty well. Representative images that are from three independent experiments were collected. Scale bars, 2 μm (also see Fig. S4; Movie S1).

neutralization against the WT and alpha pseudoviruses. VHH21 exhibited a highly neutralizing activity against the pseudoviruses of all SARS-CoV-2 VOCs (Fig. 4A and 4B).

To assess the VHH neutralization of S1 binding to the viral receptor ACE2, we conducted the BLI-based competition assay of the binding of monomeric ACE2 to immobilized S1 with treatment of the nanobodies. Figure 4C shows the considerable reduction in ACE2 binding to S1 with most of the candidate VHHs, consistent with the findings of PSV infection assays. However, only the S-trimer destructive VHH21 exhibited a striking additive effect for ACE2 binding to S1, which suggests that the target epitopes differ from the ACE2 binding sites (receptor binding motif, RBM) and indicates that the VHH21 broad neutralizing capacity does not stem from the inhibition of viral infection by blocking ACE2 binding but rather by destroying the S-trimer.

VHH21 targets a new epitope resistant to SARS-CoV-2 variants

To gain insights into the structure of the targeted regions, we performed single-particle cryo-EM analysis of the S-trimer complexed with the nanobodies. Cryo-EM analysis of the WT SARS-CoV-2 S cross-linked in advance to complex with VHH21 revealed that approximately 74% of the complexes comprised one S-trimer bound to two VHH21 molecules, which resulted in a density map at 3.3 Å resolution (Fig. S6). The S-trimer adopted a partially open prefusion architecture, with two of the three RBDs in a closed conformation and the third RBD in a half-up conformation between the up and down states (Figs. 5A and S7A). One VHH21 molecule was bound to the half-up RBD, and the other interacted with the adjacent counterclockwise RBD in the down conformation (Fig. 5A). Both VHH21 molecules occupied the loops extended to the right from the antiparallel β sheet at the edge of the core subdomain with an orientation cross-over to the ridge of the RBD (Fig. 5B and 5C). Although the VHH21 molecule bound to the half-up RBD displayed flexibility, the structure of VHH21 around the interface with the RBD in the down conformation was well defined in the map (Fig. S6E). To date, antibodies targeting the RBD of SARS-CoV-2 S protein can be divided into five main classes based on their binding regions on the RBD

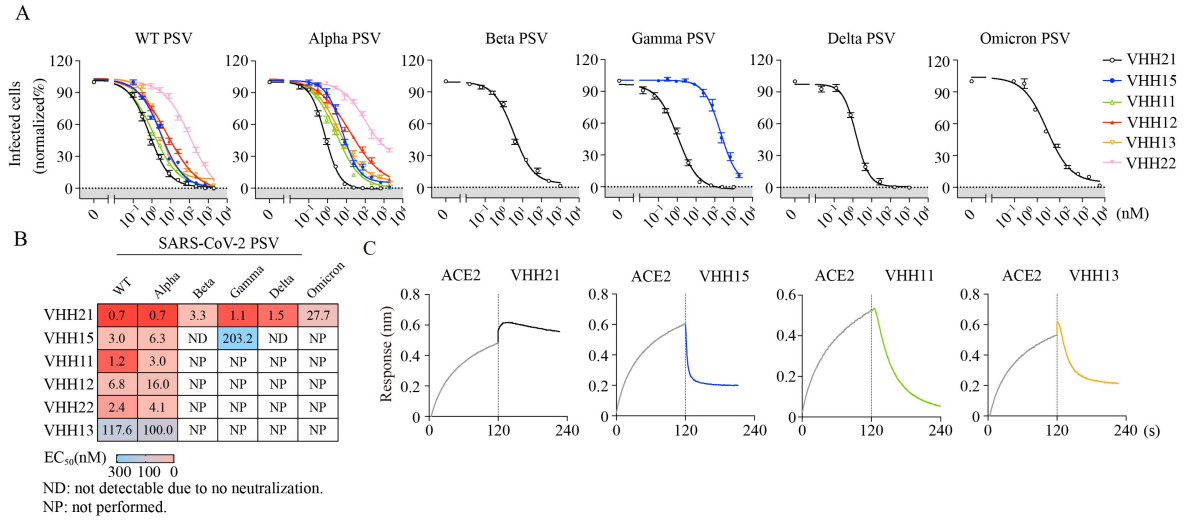

Fig. 4 Nanobodies neutralized the pseudoviruses of the coronavirus S protein via different mechanisms. (A) Neutralization curves of the VHHs. Coronaviruses S PSV sufficient to generate ~100 000 RLUs was incubated with a dilution series of the nanobodies at 37 °C for 1 h, followed by infection of 293T cells that overexpress ACE2 for 48 h. The luciferase luminescence (RLU) was measured using the Bright-Glo™ Assay System (Promega), in accordance with the manufacturer's instructions, using the luminescence microplate reader Varioskan Flash (Thermo). Data are the mean ± SD of three independent experiments. (B) EC_{50} neutralization values for the experiments shown in Fig. 4A. ND: not detectable because no neutralization occurred. NP: not performed. (C) BLI response analysis of the competitive binding of VHHs to ACE2. Each sensor was immobilized with 15 μg/mL SARS-CoV-2 WT S1 protein, followed by association of ACE2 (800 nmol/L) for 120 s and then that of VHHs (200 nmol/L) for 120 s, without the dissociation process. Representative binding curves are shown from three independent experiments.

(Fig. 5B) [40,41]. Class 1 and 2 antibodies directly bind to the RBM, and class 3 and 4 antibodies target the opposing sides outside it. The more recently discovered class 5 antibodies bind to a cryptic epitope that overlaps with the NTD-interacting region. Interestingly, the VHH21 epitope was distinct from all other reported epitopes (Fig. 5B) [42]. The loop from VHH21-CDR3 turned over and bound along a groove formed by loops 345–346 and 441–450 on the outer face of the RBD (Fig. 5C). The side chain of W105 penetrated the bottom of the groove and interacted with the side chain of R346 from the RBD (Fig. 5C). In addition to CDR3, VHH21 made contact with the RBD through CDR1, FR2, and FR3 and potentially formed interactions with loop 440–445 of the RBD and P499 and T500 from the RBM on the inner ridge face (Fig. 5C). Consequently, minimal overlaps were observed between the VHH21 epitope and RBM (Figs. 5D and S7B), which indicates that VHH21 did not compete for receptor interaction (Fig. 4C). However, in the half-up RBD conformation captured in our structure, the ACE2 binding region was incompletely exposed and could not be approached because of collisions with the other VHH21 epitope bound to the neighboring RBD in a down conformation (Fig. S7B).

Similar to the complex mentioned above, approximately 26% of the complexes featured the S-trimer bound to only one VHH21 via the RBD in a completely up conformation, with the other two RBDs in the down conformation (Fig. S6). This finding suggests that at least one RBD in the up conformation is necessary for VHH21 binding. Superposition of the VHH21-bound RBD with the RBD of an all-closed S trimer revealed minor collisions between the bound VHH21 and clockwise RBD (Fig. S7C). This result indicates that VHH21 can readily bind to the dynamic RBD when the S-trimer was in motion. However, the VHH21-bound RBD could no longer transition to the down state. Furthermore, for the S-trimer in complex with two VHH21 molecules, the half-up RBD bound to VHH21 failed to transition to the down state because of steric hindrance from the clockwise RBD, and VHH21 bound to the counterclockwise RBD in the down conformation (Fig. S7D). These results reveal that for VHH21 binding, the down-conformation RBD required the clockwise RBD to transition to an up or half-up state, and the bound VHH21 assisted in maintaining the S-trimer in an open state, which potentially weakened the protein's stability.

Conserved epitopes of VHH21 in diverse coronaviruses

To investigate the broad-spectrum affinity and neutralizing capability of VHH21, we predicted the structures of VHHs complexed with RBD of SARS-CoV-2 VOCs, BatRaTG13, SARS-CoV, or MERS-CoV. The structure of the VHH21/RBD-WT resolved in this study was utilized as the template model. The epitope recognized by VHH21 excluded nearly all the mutations discovered in SARS-CoV-2 variants, including Delta and Omicron, and was conserved across the SARS-CoV-2

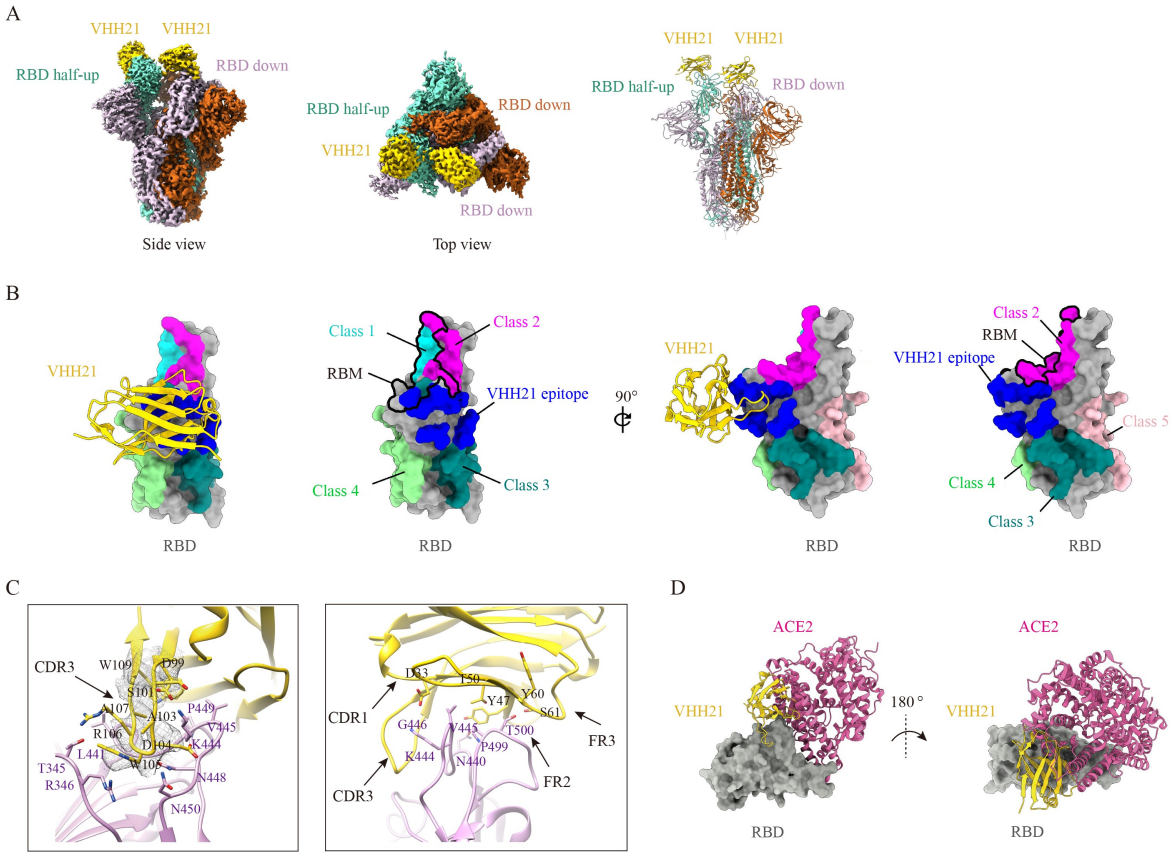

Fig. 5 Cryo-EM structure of VHH21 bound to the S-trimer. (A) Different views of the overall cryo-EM structure of the VHH21-bound S-trimer. The side view is represented by a density map and cartoon and the top view by a density map alone. Each protomer of the S-trimer is colored thistle, chocolate, and aquamarine, and VHH21 is colored gold. (B) Comparison of the VHH21 epitope with the classic class 1–5 antibody epitopes. The VHH21 structure is shown as a cartoon and colored yellow. The structure of the SARS-CoV-2 RBD is displayed as a gray surface. The VHH21 epitope and class 1–5 epitopes are colored blue, cyan, magenta, teal, green, and light pink, respectively. The outline of RBM region is presented in black. (C) Detailed interaction interface between RBD and VHH21 formed by the CDR3 (left) and CDR1, FR2, and FR3 (right) from VHH21. Potentially interacting residues at the interface are exhibited as sticks. The densities of the side chains of the CDR3 residues from the interaction regions observed in the map are conveyed as a gray mesh. (D) Structural superposition of ACE2-bound RBD (hot pink, PDB: 6M0J) to VHH21-bound RBD. The RBD is represented by a surface mode, and ACE2 and VHH21 are in cartoon mode.

VOCs (Fig. 6A). This unique binding epitope on the RBD, as identified using VHH21, holds promise in guiding the development of effective novel therapeutics for combatting a wide range of SARS-CoV-2-related coronaviruses. However, certain residue substitutions within the epitope of other coronaviruses may diminish the binding capability of VHH21 (Fig. 6A).

Moreover, in the RBDs of SARS-CoV and MERS-CoV, critical regions, including the binding loop 440–450 and that containing P499 and T500, that mediate VHH21 interaction shifted away. This structural divergence may hinder the epitope recognition by VHH21, which explains the weakened affinity and neutralization efficacy of VHH21 against SARS-CoV (Fig. 6B and 6C). Our structural prediction analysis result suggests that residue substitutions within the epitopes of other coronaviruses can affect VHH21's binding capability to varying degrees.

Discussion

Antibody catalysis studies have demonstrated that antibodies can accommodate more complex chemistry than simple binding [21]. Some antibodies can neutralize and destroy antigens [20,43]. In the present study, we introduced a novel super-resolution screening and analysis platform based on visual fluorescence probes to monitor single protein and protein subunits for the first time. This platform provides a functional screening strategy for the isolation of nanobodies that can dismantle the S-trimer, which may benefit the development of functional proteins that can catalyze the structural changes in target proteins. The quenching of fluorescently labeled antibody was the main factor that affected the observation period of the platform.

The identification of VHH21, which demonstrated the remarkably rapid and efficient catalytic destruction of the

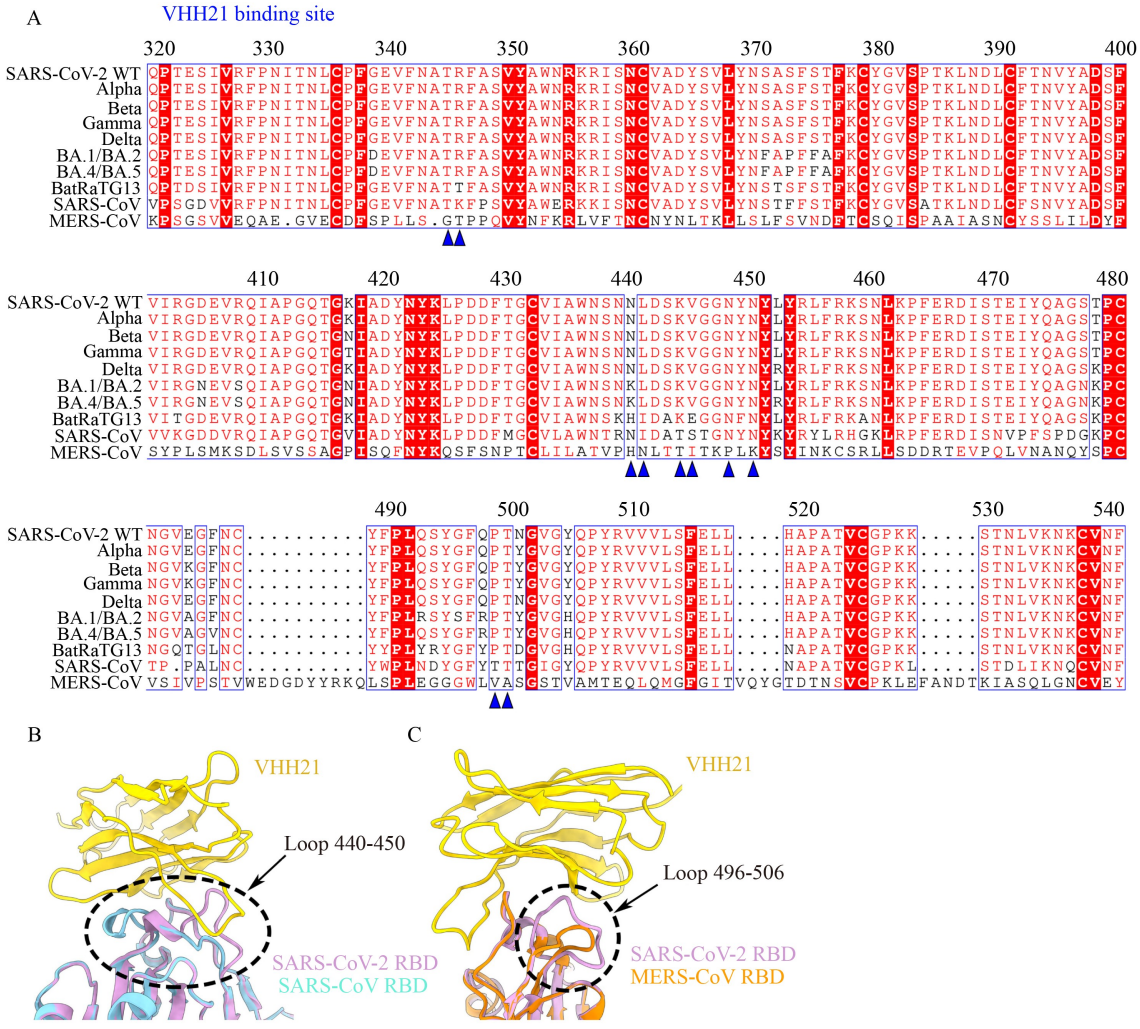

Fig. 6 Comparison of the binding epitope of various coronaviruses. (A) Sequence alignment of RBDs from SARS-CoV-2 VOCs, BatRaTG13, SARS-CoV, and MERS-CoV. The blue triangles indicate amino acids from the VHH21 epitope that potentially interact with SARS-CoV-2 RBD. (B–C) Structural comparisons of VHH21 (yellow) bound to SARS-CoV-2 RBD (pink) with SARS-CoV RBD (blue) or MERS-CoV RBD (orange).

S-trimers of SARS-CoV-2, surpassed the performance of previously reported antibodies [44,45]; in addition, it presented an important breakthrough in combating COVID-19. Based on its catalytic efficacy and swift action, VHH21 provides a crucial strategy for the prevention of coronavirus infections during COVID-19 treatment.

Nanobodies exhibit favorable biophysical and pharmacological properties for therapeutic development, including their minimal size, good stability, reversible refolding, excellent solubility, specific recognition of unique epitopes with subnanomolar affinity, and amenability to engineering [46–51]. To curb the ongoing pandemic and shield against current and future circulating SARS-CoV-2 variants, we can use highly selective neutralizing nanobodies and multivalent VHH forms as versatile alternatives to existing vaccines [52–55]. In addition to their catalytic function, our neutralizing nanobodies exhibited a high binding affinity toward S1 and different levels of cross-reactivity with SARS-CoV-2 VOCs, BatRaTG13, and SARS-CoV. We validated the inhibitory activity of VHH21 *in vitro* using lentivirus pseudoviruses with various recognition and neutralizing characteristics. VHH21 exhibited ultrahigh binding and neutralizing affinity toward the highly transmissible Alpha variant while retaining various neutralizing capability toward the highly escapable Beta, Gamma, and Omicron variants [2,15,56]. Notably, the DNA sequences encoding the S1 proteins and S pseudovirus contain as many mutations derived from the same subvariant as possible (Fig. 6A; Table S4). This challenge, which differs from most of reported papers, further reflects the excellent binding capability and neutralizing affinity of VHH21. Competition assays and structural analysis

revealed that VHH21 targets highly conserved regions distant from the identified mutations and RBM epitopes of SARS-CoV-2 viruses. This finding implies that VHH21 has the potential to be an effective tool against infections caused by several sarbecoviruses.

Bivalent nanobodies induce the slow activation of the S protein, which leads to irreversible conformational changes that drive the protein to adopt the energetically favorable postfusion conformation [44,45]. These changes mimic the interaction of the prefusion protein with membrane ACE2, which suppresses viral mutational escape. In addition to aberrant activation of the S protein, bivalent nanobodies compete with ACE2 for binding and collectively contribute to its neutralizing activity. Our study demonstrated that VHH21 can spontaneously undergo dimerization (Fig. S1) and display substantially better neutralizing activity against pseudoviruses than the other five monomeric nanobodies with similar or stronger affinity toward the S1 proteins of Alpha and Delta variants (Figs. 1F, 4A, and 4B; Table S3). The findings indicate that similar to the artificially modified bivalent antibodies, the spontaneously dimerized VHH21 exhibits a substantially enhanced neutralization capacity, which effectively counters viral mutational escape. Furthermore, the observed formation of snowflake S1/VHH complexes in confocal images was attributed to the spontaneous dimerization of VHH21.

Structural analysis revealed that three bivalent naonobodies were needed to stabilize the S protein in the 3-up conformation [45]. Typically, the native S-trimer is predominantly found in a 3-down or 1-up conformation, and most of the antibodies and nanobodies can only interact with the S protein when the RBDs are in the up position. However, VHH21 bound to the RBD without the requirement for a full-up conformation, which led to an efficient catalytic activity. In the fluorescence super-resolution imaging experiments, a considerable proportion of the S1 subunits rapidly dissociated from the S-trimer immediately within 50 ms after the treatment involving the developed nanobody. This result indicates rapid and efficient conformational catalysis, which occurred considerably earlier than infection. Altogether, our findings reveal that VHH21 destroys viral S proteins by catalyzing irreversible conformational changes and swiftly and effectively disables the S fusion machinery to render the virus inactive prior to infection.

In summary, we introduced a novel super-resolution screening and analysis platform for the first time, and it may benefit the development of functional nanobodies for the catalysis of structural changes in target proteins. Our study unveiled a new nanoabzyme, VHH21, distinguished by its catalytic prowess in the disassembly of the S-trimer of SARS-CoV-2. Leveraging spontaneous dimerization, VHH21 showcased a remarkable binding affinity and potent neutralizing capabilities across diverse variants. This novel mechanism presents a promising avenue for combating a broad spectrum of SARS-CoV-2 variants and infections caused by various coronaviruses.

Acknowledgements

We thank Xiaojun Huang, Boling Zhu, Lihong Chen, Xujing Li, Dong Li, Zhensheng Xie at the Center for Biological Imaging, Core Facilities for protein Science and Yuanyuan Chen, Zhenwei Yang and Bingxue Zhou (IBP, CAS) for technical assistance, Wei Zhang, Dong Qi and Xuefen Zhang at the OptoFem Tech. Limited for the instrument demonstrations of Abberior STEDYCON nanoscopes. This work was supported by grants from National Natural Science Foundation of China (Nos. 92374206, 82225037, 31900871, and 32241027), National Key R&D Program of China (Nos. 2022YFA1303602 and 2021YFA1301402), the Strategic Priority Research Program of CAS (Nos. XDB37030206, XDB29040102, XDB37040101, and XDB29030103), Shanghai Municipal Science and Technology Major Project (No. ZD2021CY001), Basic Research Program Based on Major Scientific Infrastructures of CAS (No. JZHKYPT-2021-05), Key Laboratory of Biomacromolecules of CAS (No. ZGD-2023-05), Beijing Nova Program (No. 20230484239 to Duanfang Cao).

Compliance with ethics guidelines

Conflicts of interest Kai Wang, Duanfang Cao, Lanlan Liu, Xiaoyi Fan, Yihuan Lin, Wenting He, Yunze Zhai, Pingyong Xu, Xiyun Yan, Haikun Wang, Xinzheng Zhang, and Pengyuan Yang declare that no competing interests were involved in this work.

The experimental procedures for use and care of animals were approved by the ethics committee of Institute of Biophysics, Chinese Academy of Sciences. All institutional and national guidelines for the care and use of laboratory animals were followed.

Electronic Supplementary Material Supplementary material is available in the online version of this article at https://doi.org/10.1007/s11684-025-1128-4 and is accessible for authorized users.

References

1. Telenti A, Arvin A, Corey L, Corti D, Diamond MS, Garcia-Sastre A, Garry RF, Holmes EC, Pang PS, Virgin HW. After the pandemic: perspectives on the future trajectory of COVID-19. Nature 2021; 596(7873): 495–504
2. Cameroni E, Bowen JE, Rosen LE, Saliba C, Zepeda SK, Culap K, Pinto D, VanBlargan LA, De Marco A, di Iulio J, Zatta F, Kaiser H, Noack J, Farhat N, Czudnochowski N, Havenar-Daughton C, Sprouse KR, Dillen JR, Powell AE, Chen A, Maher C, Yin L, Sun D, Soriaga L, Bassi J, Silacci-Fregni C, Gustafsson C, Franko NM, Logue J, Iqbal NT, Mazzitelli I, Geffner J, Grifantini R, Chu H, Gori A, Riva A, Giannini O, Ceschi A, Ferrari P, Cippa PE, Franzetti-Pellanda A, Garzoni C, Halfmann PJ, Kawaoka Y,

Hebner C, Purcell LA, Piccoli L, Pizzuto MS, Walls AC, Diamond MS, Telenti A, Virgin HW, Lanzavecchia A, Snell G, Veesler D, Corti D. Broadly neutralizing antibodies overcome SARS-CoV-2 Omicron antigenic shift. Nature 2022; 602(7898): 664–670

3. Liu L, Iketani S, Guo Y, Chan JF, Wang M, Liu L, Luo Y, Chu H, Huang Y, Nair MS, Yu J, Chik KK, Yuen TT, Yoon C, To KK, Chen H, Yin MT, Sobieszczyk ME, Huang Y, Wang HH, Sheng Z, Yuen KY, Ho DD. Striking antibody evasion manifested by the Omicron variant of SARS-CoV-2. Nature 2022; 602(7898): 676–681
4. Wang Q, Iketani S, Li Z, Liu L, Guo Y, Huang Y, Bowen AD, Liu M, Wang M, Yu J, Valdez R, Lauring AS, Sheng Z, Wang HH, Gordon A, Liu L, Ho DD. Alarming antibody evasion properties of rising SARS-CoV-2 BQ and XBB subvariants. Cell 2023; 186(2): 279–286.e8
5. Jackson CB, Farzan M, Chen B, Choe H. Mechanisms of SARS-CoV-2 entry into cells. Nat Rev Mol Cell Biol 2022; 23(1): 3–20
6. Xia S, Lan Q, Su S, Wang X, Xu W, Liu Z, Zhu Y, Wang Q, Lu L, Jiang S. The role of furin cleavage site in SARS-CoV-2 spike protein-mediated membrane fusion in the presence or absence of trypsin. Signal Transduct Target Ther 2020; 5(1): 92
7. Xia S, Zhu Y, Liu M, Lan Q, Xu W, Wu Y, Ying T, Liu S, Shi Z, Jiang S, Lu L. Fusion mechanism of 2019-nCoV and fusion inhibitors targeting HR1 domain in spike protein. Cell Mol Immunol 2020; 17(7): 765–767
8. Wang PF, Nair MS, Liu LH, Iketani S, Luo Y, Guo YC, Wang M, Yu J, Zhang BS, Kwong PD, Graham BS, Mascola JR, Chang JY, Yin MT, Sobieszczyk M, Kyratsous CA, Shapiro L, Sheng ZZ, Huang YX, Ho DD. Antibody resistance of SARS-CoV-2 variants B. 1.351 and B. 1.1. 7. Nature 2021; 593(7857): 130–135
9. Chen RTE, Zhang XW, Case JB, Winkler ES, Liu Y, VanBlargan LA, Liu JY, Errico JM, Xie XP, Suryadevara N, Gilchuk P, Zost SJ, Tahan S, Droit L, Turner JS, Kim W, Schmitz AJ, Thapa M, Wang DV, Boon ACM, Presti RM, O'Halloran JA, Kim AHJ, Deepak P, Pinto D, Fremont DH, Crowe JE Jr, Corti D, Virgin HW, Ellebedy AH, Shi PY, Diamond MS. Resistance of SARS-CoV-2 variants to neutralization by monoclonal and serum-derived polyclonal antibodies. Nat Med 2021; 27(4): 717–726
10. Hanke L, Vidakovics Perez L, Sheward DJ, Das H, Schulte T, Moliner-Morro A, Corcoran M, Achour A, Karlsson Hedestam GB, Hällberg BM, Murrell B, McInerney GM. An alpaca nanobody neutralizes SARS-CoV-2 by blocking receptor interaction. Nat Commun 2020; 11(1): 4420
11. Huo J, Le Bas A, Ruza RR, Duyvesteyn HME, Mikolajek H, Malinauskas T, Tan TK, Rijal P, Dumoux M, Ward PN, Ren J, Zhou D, Harrison PJ, Weckener M, Clare DK, Vogirala VK, Radecke J, Moynié L, Zhao Y, Gilbert-Jaramillo J, Knight ML, Tree JA, Buttigieg KR, Coombes N, Elmore MJ, Carroll MW, Carrique L, Shah PNM, James W, Townsend AR, Stuart DI, Owens RJ, Naismith JH. Neutralizing nanobodies bind SARS-CoV-2 spike RBD and block interaction with ACE2. Nat Struct Mol Biol 2020; 27(9): 846–854
12. Wrapp D, De Vlieger D, Corbett KS, Torres GM, Wang N, Van Breedam W, Roose K, van Schie L, Hoffmann M, Pöhlmann S, Graham BS, Callewaert N, Schepens B, Saelens X, McLellan JS. Structural basis for potent neutralization of betacoronaviruses by single-domain camelid antibodies. Cell 2020; 181(5): 1004–1015.e15
13. Chi X, Liu X, Wang C, Zhang X, Li X, Hou J, Ren L, Jin Q, Wang J, Yang W. Humanized single domain antibodies neutralize SARS-CoV-2 by targeting the spike receptor binding domain. Nat Commun 2020; 11(1): 4528
14. Li C, Zhan W, Yang Z, Tu C, Hu G, Zhang X, Song W, Du S, Zhu Y, Huang K, Kong Y, Zhang M, Mao Q, Gu X, Zhang Y, Xie Y, Deng Q, Song Y, Chen Z, Lu L, Jiang S, Wu Y, Sun L, Ying T. Broad neutralization of SARS-CoV-2 variants by an inhalable bispecific single-domain antibody. Cell 2022; 185(8): 1389–1401.e18
15. Planas D, Saunders N, Maes P, Guivel-Benhassine F, Planchais C, Buchrieser J, Bolland WH, Porrot F, Staropoli I, Lemoine F, Pere H, Veyer D, Puech J, Rodary J, Baela G, Dellicour S, Raymenants J, Gorissen S, Geenen C, Vanmechelen B, Wawina-Bokalanga T, Marti-Carrerasi J, Cuypers L, Seve A, Hocqueloux L, Prazuck T, Rey F, Simon-Lorriere E, Bruel T, Mouquet H, Andre E, Schwartz O. Considerable escape of SARS-CoV-2 Omicron to antibody neutralization. Nature 2022; 602(7898): 671–675
16. Cao YL, Wang J, Jian FC, Xiao TH, Song WL, Yisimayi A, Huang WJ, Li QQ, Wang P, An R, Wang Y, Niu X, Yang SJ, Liang H, Sun HY, Li T, Yu YL, Cui QQ, Liu S, Yang XD, Du S, Zhang ZY, Hao XH, Shao F, Jin RH, Wang XX, Xiao JY, Wang YC, Xie XS. Omicron escapes the majority of existing SARS-CoV-2 neutralizing antibodies. Nature 2022; 602(7898): 657–663
17. Cui Z, Liu P, Wang N, Wang L, Fan K, Zhu Q, Wang K, Chen R, Feng R, Jia Z, Yang M, Xu G, Zhu B, Fu W, Chu T, Feng L, Wang Y, Pei X, Yang P, Xie XS, Cao L, Cao Y, Wang X. Structural and functional characterizations of infectivity and immune evasion of SARS-CoV-2 Omicron. Cell 2022; 185(5): 860–871.e13
18. Su Y, Yuan D, Chen DG, Ng RH, Wang K, Choi J, Li S, Hong S, Zhang R, Xie J, Kornilov SA, Scherler K, Pavlovitch-Bedzyk AJ, Dong S, Lausted C, Lee I, Fallen S, Dai CL, Baloni P, Smith B, Duvvuri VR, Anderson KG, Li J, Yang F, Duncombe CJ, McCulloch DJ, Rostomily C, Troisch P, Zhou J, Mackay S, DeGottardi Q, May DH, Taniguchi R, Gittelman RM, Klinger M, Snyder TM, Roper R, Wojciechowska G, Murray K, Edmark R, Evans S, Jones L, Zhou Y, Rowen L, Liu R, Chour W, Algren HA, Berrington WR, Wallick JA, Cochran RA, Micikas ME, Wrin T, Petropoulos CJ, Cole HR, Fischer TD, Wei W, Hoon DSB, Price ND, Subramanian N, Hill JA, Hadlock J, Magis AT, Ribas A, Lanier LL, Boyd SD, Bluestone JA, Chu H, Hood L, Gottardo R, Greenberg PD, Davis MM, Goldman JD, Heath JR. Multiple early factors anticipate post-acute COVID-19 sequelae. Cell 2022; 185(5): 881–895.e20
19. Davies NG, Abbott S, Barnard RC, Jarvis CI, Edmunds WJ. Estimated transmissibility and impact of SARS-CoV-2 lineage B. 1.1. 7 in England. Science 2021; 372(6538): eabg3055
20. Ma Y, Mao Q, Wang Y, Zhang Z, Chen J, Hao A, Rehati P, Wang Y, Wen Y, Lu L, Chen Z, Zhao J, Wu F, Sun L, Huang J. A broadly neutralizing antibody inhibits SARS-CoV-2 variants through a novel mechanism of disrupting spike trimer integrity. Cell Res 2023; 33(12): 975–978
21. Mahendra A, Sharma M, Rao DN, Peyron I, Planchais C, Dimitrov JD, Kaveri SV, Lacroix-Desmazes S. Antibody-mediated catalysis: induction and therapeutic relevance. Autoimmun Rev 2013; 12(6): 648–652
22. Xu B, Wang K, Vasylieva N, Zhou H, Xue X, Wang B, Li QX, Hammock BD, Xu T. Development of a nanobody-based ELISA

for the detection of the insecticides cyantraniliprole and chlorantraniliprole in soil and the vegetable bok choy. Anal Bioanal Chem 2021; 413(9): 2503–2511

23. Kim HJ, McCoy MR, Majkova Z, Dechant JE, Gee SJ, Tabares-da Rosa S, González-Sapienza GG, Hammock BD. Isolation of alpaca anti-hapten heavy chain single domain antibodies for development of sensitive immunoassay. Anal Chem 2012; 84(2): 1165–1171
24. Wang K, Vasylieva N, Wan DB, Eads DA, Yang J, Tretten T, Barnych B, Li J, Li QX, Gee SJ, Hammock BD, Xu T. Quantitative detection of fipronil and fipronil-sulfone in sera of black-tailed prairie dogs and rats after oral exposure to fipronil by camel single-domain antibody-based immunoassays. Anal Chem 2019; 91(2): 1532–1540
25. Ingram JR, Schmidt FI, Ploegh HL. Exploiting nanobodies' singular traits. Annu Rev Immunol 2018; 36(1): 695–715
26. Fan X, Cao D, Kong L, Zhang X. Cryo-EM analysis of the post-fusion structure of the SARS-CoV spike glycoprotein. Nat Commun 2020; 11(1): 3618
27. Liu A, Huang X, He W, Xue F, Yang Y, Liu J, Chen L, Yuan L, Xu P. pHmScarlet is a pH-sensitive red fluorescent protein to monitor exocytosis docking and fusion steps. Nat Commun 2021; 12(1): 1413
28. Wu CL, Huang XJ, Cheng J, Zhu DJ, Zhang XZ. High-quality, high-throughput cryo-electron microscopy data collection via beam tilt and astigmatism-free beam-image shift. J Struct Biol 2019; 208(3): 107396
29. Zheng SQ, Palovcak E, Armache JP, Verba KA, Cheng Y, Agard DA. MotionCor2: anisotropic correction of beam-induced motion for improved cryo-electron microscopy. Nat Methods 2017; 14(4): 331–332
30. Rohou A, Grigorieff N. CTFFIND4: fast and accurate defocus estimation from electron micrographs. J Struct Biol 2015; 192(2): 216–221
31. Scheres SH. RELION: implementation of a bayesian approach to cryo-EM structure determination. J Struct Biol 2012; 180(3): 519–530
32. Kucukelbir A, Sigworth FJ, Tagare HD. Quantifying the local resolution of cryo-EM density maps. Nat Methods 2014; 11(1): 63–65
33. Jumper J, Evans R, Pritzel A, Green T, Figurnov M, Ronneberger O, Tunyasuvunakool K, Bates R, Žídek A, Potapenko A, Bridgland A, Meyer C, Kohl SAA, Ballard AJ, Cowie A, Romera-Paredes B, Nikolov S, Jain R, Adler J, Back T, Petersen S, Reiman D, Clancy E, Zielinski M, Steinegger M, Pacholska M, Berghammer T, Bodenstein S, Silver D, Vinyals O, Senior AW, Kavukcuoglu K, Kohli P, Hassabis D. Highly accurate protein structure prediction with AlphaFold. Nature 2021; 596(7873): 583–589
34. Pettersen EF, Goddard TD, Huang CC, Couch GS, Greenblatt DM, Meng EC, Ferrin TE. UCSF Chimera–a visualization system for exploratory research and analysis. J Comput Chem 2004; 25(13): 1605–1612
35. Emsley P, Lohkamp B, Scott WG, Cowtan K. Features and development of Coot. Acta Crystallogr D Biol Crystallogr 2010; 66(4): 486–501
36. Adams PD, Afonine PV, Bunkoczi G, Chen VB, Davis IW, Echols N, Headd JJ, Hung LW, Kapral GJ, Grosse-Kunstleve RW, McCoy AJ, Moriarty NW, Oeffner R, Read RJ, Richardson DC, Richardson JS, Terwilliger TC, Zwart PH. PHENIX: a comprehensive python-based system for macromolecular structure solution. Acta Crystallogr D Biol Crystallogr 2010; 66(Pt 2): 213–221
37. Chen VB, Arendall WB III, Headd JJ, Keedy DA, Immormino RM, Kapral GJ, Murray LW, Richardson JS, Richardson DC. MolProbity: all-atom structure validation for macromolecular crystallography. Acta Crystallogr D Biol Crystallogr 2010; 66(1): 12–21
38. Wrobel AG, Benton DJ, Xu P, Roustan C, Martin SR, Rosenthal PB, Skehel JJ, Gamblin SJ. SARS-CoV-2 and bat RaTG13 spike glycoprotein structures inform on virus evolution and furin-cleavage effects. Nat Struct Mol Biol 2020; 27(8): 763–767
39. Crawford K, Eguia R, Dingens AS, Loes AN, Bloom JD. Protocol and reagents for pseudotyping lentiviral particles with SARS-CoV-2 spike protein for neutralization Assays. Viruses 2020; 12(5): 513
40. Cui L, Li T, Xue W, Zhang S, Wang H, Liu H, Gu Y, Xia N, Li S. Comprehensive overview of broadly neutralizing antibodies against SARS-CoV-2 variants. Viruses 2024; 16(6): 900
41. Barnes CO, Jette CA, Abernathy ME, Dam KA, Esswein SR, Gristick HB, Malyutin AG, Sharaf NG, Huey-Tubman KE, Lee YE, Robbiani DF, Nussenzweig MC, West AP Jr, Bjorkman PJ. SARS-CoV-2 neutralizing antibody structures inform therapeutic strategies. Nature 2020; 588(7839): 682–687
42. Hastie KM, Li H, Bedinger D, Schendel SL, Dennison SM, Li K, Rayaprolu V, Yu X, Mann C, Zandonatti M, Diaz Avalos R, Zyla D, Buck T, Hui S, Shaffer K, Hariharan C, Yin J, Olmedillas E, Enriquez A, Parekh D, Abraha M, Feeney E, Horn GQ, Aldon Y, Ali H, Aracic S, Cobb RR, Federman RS, Fernandez JM, Glanville J, Green R, Grigoryan G, Lujan Hernandez AG, Ho DD, Huang KYA, Ingraham J, Jiang W, Kellam P, Kim C, Kim M, Kim HM, Kong C, Krebs SJ, Lan F, Lang G, Lee S, Leung CL, Liu J, Lu Y, MacCamy A, McGuire AT, Palser AL, Rabbitts TH, Rikhtegaran Tehrani Z, Sajadi MM, Sanders RW, Sato AK, Schweizer L, Seo J, Shen B, Snitselaar JL, Stamatatos L, Tan Y, Tomic MT, van Gils MJ, Youssef S, Yu J, Yuan TZ, Zhang Q, Peters B, Tomaras GD, Germann T, Saphire EO. Defining variant-resistant epitopes targeted by SARS-CoV-2 antibodies: a global consortium study. Science 2021; 374(6566): 472–478
43. Wentworth AD, Jones LH, Wentworth P Jr, Janda KD, Lerner RA. Antibodies have the intrinsic capacity to destroy antigens. Proc Natl Acad Sci USA 2000; 97(20): 10930–10935
44. Wang X, Chen X, Tan J, Yue S, Zhou R, Xu Y, Lin Y, Yang Y, Zhou Y, Deng K, Chen Z, Ye L, Zhu Y. 35B5 antibody potently neutralizes SARS-CoV-2 Omicron by disrupting the N-glycan switch via a conserved spike epitope. Cell Host Microbe 2022; 30(6): 887–895.e4
45. Koenig PA, Das H, Liu HJ, Kummerer BM, Gohr FN, Jenster LM, Schiffelers LDJ, Tesfamariam YM, Uchima M, Wuerth JD, Gatterdam K, Ruetalo N, Christensen MH, Fandrey CI, Normann S, Todtmann JMP, Pritzl S, Hanke L, Boos J, Yuan M, Zhu XY, Schmid-Burgk JL, Kato H, Schindler M, Wilson IA, Geyer M, Ludwig KU, Hallberg BM, Wu NC, Schmidt FI. Structure-guided multivalent nanobodies block SARS-CoV-2 infection and suppress mutational escape. Science 2021; 371(6530): eabe6230
46. Vincke C, Loris R, Saerens D, Martinez-Rodriguez S, Muyldermans S, Conrath K. General strategy to humanize a camelid single-domain antibody and identification of a universal humanized nanobody scaffold. J Biol Chem 2009; 284(5):

3273–3284
47. Beirnaert E, Desmyter A, Spinelli S, Lauwereys M, Aarden L, Dreier T, Loris R, Silence K, Pollet C, Cambillau C, de Haard H. Bivalent llama single-domain antibody fragments against tumor necrosis factor have picomolar potencies due to intramolecular interactions. Front Immunol 2017; 8: 867
48. Holliger P, Hudson PJ. Engineered antibody fragments and the rise of single domains. Nat Biotechnol 2005; 23(9): 1126–1136
49. Siontorou CG. Nanobodies as novel agents for disease diagnosis and therapy. Int J Nanomedicine 2013; 8: 4215–4227
50. De Meyer T, Muyldermans S, Depicker A. Nanobody-based products as research and diagnostic tools. Trends Biotechnol 2014; 32(5): 263–270
51. Muyldermans S. Nanobodies: natural single-domain antibodies. Annu Rev Biochem 2013; 82(1): 775–797
52. Bracken CJ, Lim SA, Solomon P, Rettko NJ, Nguyen DP, Zha BS, Schaefer K, Byrnes JR, Zhou J, Lui I, Liu J, Pance K; QCRG Structural Biology Consortium; Zhou XX, Leung KK, Wells JA. Bi-paratopic and multivalent VH domains block ACE2 binding and neutralize SARS-CoV-2. Nat Chem Biol 2021; 17(1): 113–121
53. Schoof M, Faust B, Saunders RA, Sangwan S, Rezelj V, Hoppe N, Boone M, Billesbølle CB, Puchades C, Azumaya CM, Kratochvil HT, Zimanyi M, Deshpande I, Liang J, Dickinson S, Nguyen HC, Chio CM, Merz GE, Thompson MC, Diwanji D, Schaefer K, Anand AA, Dobzinski N, Zha BS, Simoneau CR, Leon K, White KM, Chio US, Gupta M, Jin M, Li F, Liu Y, Zhang K, Bulkley D, Sun M, Smith AM, Rizo AN, Moss F, Brilot AF, Pourmal S, Trenker R, Pospiech T, Gupta S, Barsi-Rhyne B, Belyy V, Barile-Hill AW, Nock S, Liu Y, Krogan NJ, Ralston CY, Swaney DL, García-Sastre A, Ott M, Vignuzzi M; QCRG Structural Biology Consortium; Walter P, Manglik A. An ultrapotent synthetic nanobody neutralizes SARS-CoV-2 by stabilizing inactive Spike. Science 2020; 370(6523): 1473–1479
54. Xiang YF, Nambulli S, Xiao ZY, Liu H, Sang Z, Duprex WP, Schneidman-Duhovny D, Zhang C, Shi Y. Versatile and multivalent nanobodies efficiently neutralize SARS-CoV-2. Science 2020; 370(6523): 1479–1484
55. Lu QZ, Zhang ZL, Li HX, Zhong KH, Zhao Q, Wang Z, Wu ZG, Yang DH, Sun S, Yang NA, Zheng MJ, Chen Q, Long C, Guo WH, Yang H, Nie CL, Tong AP. Development of multivalent nanobodies blocking SARS-CoV-2 infection by targeting RBD of spike protein. J Nanobiotechnology 2021; 19(1): 33
56. Cao Y, Wang J, Jian F, Xiao T, Song W, Yisimayi A, Huang W, Li Q, Wang P, An R, Wang J, Wang Y, Niu X, Yang S, Liang H, Sun H, Li T, Yu Y, Cui Q, Liu S, Yang X, Du S, Zhang Z, Hao X, Shao F, Jin R, Wang X, Xiao J, Wang Y, Xie XS. Omicron escapes the majority of existing SARS-CoV-2 neutralizing antibodies. Nature 2022; 602(7898): 657–663